AGU PUBLICATIONS

JGR

Journal of Geophysical Research: Space Physics

RESEARCH ARTICLE

10.1002/2014JA020553

Key Points:
- Potential and auroral patterns affect neutral flow patterns in the thermosphere
- Latitude of the ionospheric dynamo must be correctly defined to simulate flows
- Modeled temperature is dependent on the drivers used to model the region

Correspondence to:
L. R. Liuzzo,
lukelzzo@umich.edu

Citation:
Liuzzo, L. R., A. J. Ridley, N. J. Perlongo, E. J. Mitchell, M. Conde, D. L. Hampton, W. A. Bristow, and M. J. Nicolls (2015), High-latitude ionospheric drivers and their effects on wind patterns in the thermosphere, *J. Geophys. Res. Space Physics*, *120*, 715–735, doi:10.1002/2014JA020553.

Received 28 AUG 2014
Accepted 30 NOV 2014
Accepted article online 4 DEC 2014
Published online 22 JAN 2015

High-latitude ionospheric drivers and their effects on wind patterns in the thermosphere

L. R. Liuzzo[1,2], A. J. Ridley[1], N. J. Perlongo[1], E. J. Mitchell[3], M. Conde[4], D. L. Hampton[4], W. A. Bristow[5], and M. J. Nicolls[6]

[1]Department of Atmospheric, Oceanic and Space Sciences, University of Michigan, Ann Arbor, Michigan, USA, [2]School of Earth and Atmospheric Sciences, Georgia Institute of Technology, Atlanta, Georgia, USA, [3]Johns Hopkins University Applied Physics Laboratory, Baltimore, Maryland, USA, [4]Geophysical Institute, University of Alaska Fairbanks, Fairbanks, Alaska, USA, [5]Department of Electrical and Computer Engineering, University of Alaska Fairbanks, Fairbanks, Alaska, USA, [6]Center for Geospace Studies, SRI International, Menlo Park, California, USA

Abstract Winds in the thermosphere are highly important for transporting mass, momentum, and energy over the globe. In the high-latitude region, observations show that ion and neutral motions are strongly coupled when the aurora is present but the coupling is less evident when there is no aurora. In this study, we investigate the ability of the Global Ionosphere-Thermosphere Model (GITM) to simulate the mesoscale wind structure over Alaska during a substorm. Thirteen distinct numerical simulations of a substorm event that occurred between 02:00 and 17:00 Universal Time on 24 November 2012 have been performed. Distinct drivers considered include the Weimer and SuperDARN potential patterns and the OVATION Prime and OVATION-SME auroral models. The effects of the boundary between the neutral wind dynamo calculation and the high-latitude imposed electric potential were also considered. Neutral wind velocities and thermospheric temperatures measured by the Scanning Doppler Imager instruments located at three locations in Alaska were compared to GITM simulation results, and electron densities within GITM were compared to data from the Poker Flat Incoherent Scatter Radar. It was found that the different drivers used between multiple simulations lead to various amounts of momentum coupling within the simulation, affecting the accuracy of the modeled neutral and ion flow patterns and the strength of electron precipitation at high latitudes. This affirms that better observations of auroral precipitation and electric fields are required to accurately understand and consistently reproduce the mesoscale neutral wind flow patterns and temperature structure in the high-latitude thermosphere.

1. Introduction

Understanding the interaction between the thermosphere and ionosphere is highly important in order to describe the dynamics of either region. One significant effect of the coupling between the two fluids is the modification of the thermospheric wind patterns which, without the ionospheric drag or Coriolis forces, would flow from the dayside to the nightside of the planet. It is well understood that during times of heightened geomagnetic activity, electrons precipitate into the lower layers of the thermosphere in the auroral zone, resulting in enhanced ion-neutral coupling through the ion drag force that strongly controls the neutral winds [*Meriwether et al.*, 1973; *Heppner and Miller*, 1982; *Killeen and Roble*, 1984, 1986; *Deng and Ridley*, 2006]. To better understand this complex behavior, there are many models that simulate various relationships between the charged and neutral environments in our upper atmosphere. These models include empirical models like the Mass Spectrometer and Incoherent Scatter model [*Hedin*, 1983, 1987, 1991], the International Reference Ionosphere model [*Rawer et al.*, 1978; *Bilitza*, 2001], the Horizontal Wind Model [*Hedin et al.*, 1988; *Hedin*, 1992; *Hedin et al.*, 1996; *Drob et al.*, 2008], and the Vector Spherical Harmonic model [*Killeen et al.*, 1987], data assimilation models like the Global Assimilation of Ionospheric Measurements model [*Schunk et al.*, 2004], and physics-based general circulation models presented in [*Dickinson et al.* 1984], the Thermosphere-Ionosphere General Circulation Model [*Roble et al.*, 1988], the Thermosphere-Ionosphere-Electrodynamics General Circulation Model [*Richmond et al.*, 1992], the Thermosphere-Ionosphere-Mesosphere Electrodynamics General Circulation Model [*Roble and Ridley*, 1994], the Coupled Thermosphere-Ionosphere Plasmasphere model [*Fuller-Rowell and Rees*, 1980], the Coupled Thermosphere-Ionosphere Plasmasphere Electrodynamics model [*Millward et al.*, 2001], and the Global Ionosphere-Thermosphere Model [*Ridley et al.*, 2006]. Multiple studies have

compared winds predicted by models with data from satellites [*McCormac et al.*, 1987; *Killeen et al.*, 1987; *Lathuillère et al.*, 1997; *Zhang and Shepherd*, 2000; *Richmond et al.*, 2003] and ground-based instruments [*Aruliah et al.*, 1991; *Niciejewski et al.*, 1994; *Killeen et al.*, 1995; *Niciejewski et al.*, 1996; *Emmert et al.*, 2006a, 2006b], and some have compared results to winds measured by sounding rockets [*Rothwell et al.*, 1974; *Mikkelsen et al.*, 1981]. These studies observe neutral convection patterns in order to better understand the behavior of the winds. In this study, the Global Ionosphere-Thermosphere Model (GITM) is used to explore the coupling of charged and neutral particles in the upper atmosphere auroral zone in a more detailed and rigorous manner, and to describe a more accurate response of the neutral winds to these particles.

GITM is a fully parallel, nonhydrostatic three-dimensional model that is driven by external forcing models at its upper and lower boundaries. For example, at its lower boundary, tidal structures are input from lower atmospheric models, whereas at its upper boundary, the model is forced by high-latitude electric potential and auroral precipitation patterns. There are a wide variety of sources for these models. This study focuses on the use of different high-latitude ionospheric drivers within GITM and the effect that these drivers have on neutral winds in the auroral zone. By using different representations of the electric field and auroral precipitation drivers in GITM, we are able to model the wind patterns in the thermosphere to varying degrees of accuracy, with the overall model accuracy highly dependent on each of the external drivers.

2. Methods

Wind patterns were obtained from 13 different GITM simulations of a substorm that occurred between the hours of 02:00 and 17:00 Universal Time (UT) on 24 November 2012. Each run simulation differed in the high-latitude electric potential pattern and/or auroral precipitation pattern that was used to drive ionospheric dynamics. The entire list of GITM runs can be found in Table 1. For this set of simulations, the models used a high-resolution grid spacing of 0.833° latitude by 5° longitude. While using high resolution does not intrinsically add additional physics within the model, nor does it always necessarily increase the accuracy of the modeled ion and neutral flow patterns, it does allow for sharper gradients to be more thoroughly resolved. Because abrupt changes in ion and neutral flows can often occur over small spatial scales, a high-resolution grid is used so that these gradients will be better resolved, with the intent to better represent the smallscale and midscale convection patterns for electrons, ions, and neutrals in the system. This, in turn, would ideally permit a more accurate portrayal of the response of the ionosphere-thermosphere system to various model parameters.

In order to sustain the atmosphere within GITM, the Mass Spectrometer and Incoherent Radar (MSIS) model [*Hedin*, 1983, 1987, 1991] is used to specify the density and temperature at the lower boundary, while the Horizontal Wind Model [*Drob et al.*, 2008] is used to specify the horizontal wind patterns. The values are specified in two ghost cells below 100 km altitude and are used in the advective scheme as well as any place in the code that needs a vertical gradient profile (e.g., thermal conduction). MSIS contains diurnal, semidiurnal, and tridiurnal migrating tides in the densities and temperatures, and are therefore included in the lower boundary of GITM. The HWM also contains tidal structures that are relatively consistent with the MSIS tides. *Vichare et al.* [2012] showed that these tides drive neutral winds in the lower thermosphere that power the equatorial electrojet within GITM. It is also possible in GITM to use the mean value of the temperatures and densities from MSIS and the tidal perturbations on the temperatures and winds by assuming a net horizontal wind of zero, specified by the Global-Scale Wave Model [*Hagan et al.*, 1995]; however, for this study, the MSIS and HWM tidal structures were used. In addition, the low-latitude dynamo described by *Vichare et al.* [2012] was run with a high-latitude boundary at 70° magnetic latitude unless otherwise noted. Finally, although multiple solar EUV models exist and can be used with GITM (see *Solomon and Qian* [2005] or *Chamberlin et al.* [2007]), all simulations presented here used conditions determined by the EUV flux model for aeronomic calculations [*Richards et al.*, 1994], given the $F_{10.7}$ and 81 day averaged $F_{10.7}$.

2.1. Ionospheric Drivers

GITM uses various drivers to model behaviors of the thermosphere and ionosphere under quiet and storm conditions. Two of the important drivers used by GITM are the high-latitude electric potential and auroral precipitation patterns. Generally, the drivers most commonly used with GITM have been Weimer potential patterns [*Weimer*, 2005] coupled with Fuller-Rowell and Evans auroral patterns, henceforth referred to as NOAA aurora [*Fuller-Rowell and Evans*, 1987]. The interplanetary magnetic field (IMF) measured by the ACE satellite was used to drive the Weimer potential patterns, while the NOAA Polar-orbiting Operational

Table 1. Description of Each Simulation of the Event, Along With Which Drivers Were Used, Their Abbreviations, Zonal (E/W) and Meridional (N/S) Root-Mean-Square Error (RMSE) and Mean Difference (Diff) Between the GITM and Scanning Doppler Imager (SDI) Neutral Winds (in Units of m/s), and the Directionally Averaged Root-Mean-Square Error and Mean Difference Between the GITM and SDI Temperatures (in Units of Kelvin)[a]

	Auroral		Zonal		Meridional		Temperature	
ϕ	Precipitation	Abbreviation	RMSE	<Diff>	RMSE	<Diff>	RMSE	<Diff>
W[b]	N/A	Baseline	191.8	*156.4*	**59.6**	14.0	*211.8*	*−205.1*
W	NOAA	WN	**82.7**	16.0	*141.4*	*110.2*	73.7	−29.7
W	NOAA	WND[e]	169.5	105.4	104.7	55.1	**71.9**	−29.9
SD	O Prime[c]	SdOp	121.9	**5.6**	107.8	71.0	116.6	−103.0
SD	O Prime[c]	SdOpD[e]	*198.6*	97.6	89.8	−22.2	115.0	−102.0
SD	O Prime[c]	SdOpD50[f]	169.4	121.0	101.4	70.9	122.6	−109.5
SD	O Prime[d]	SdOp6m	120.3	−45.7	121.5	76.8	73.9	**−8.8**
SD	O Prime[d]	SdOp6mD50[f]	169.0	119.1	101.9	73.3	122.0	−109.0
W	O-SME	WOs	**82.7**	45.9	82.1	49.6	78.3	−46.0
W	O-SME	WOsD[e]	163.5	114.5	70.8	**5.2**	149.4	−54.7
SD	O-SME	SdOs	104.1	−12.8	119.1	81.4	94.1	32.3
SD	O-SME	SdOsD[e]	150.7	57.9	89.3	15.5	85.1	19.3
SD	O-SME	SdOsD50[f]	103.4	−13.2	122.5	85.2	93.1	31.9

[a]Negative values indicate GITM underestimated the observed values. The term ϕ represents the electric potential pattern used and W, SD, O Prime, and O-SME are abbreviations for the Weimer, SuperDARN, OVATION Prime, and OVATION-SME drivers, respectively. The results from the most (least) accurate runs are in bold (italics).
[b]Driven by constant IMF values of $B_z = -2.0$ nT, $B_y = 0.0$ nT, and $V_x = -400.0$ km/s.
[c]Running average (4 h) of interplanetary magnetic field (IMF) and solar wind data.
[d]Running average (6 min) of IMF and solar wind data.
[e]Dynamo located at 70° geomagnetic latitude.
[f]Dynamo located at 50° geomagnetic latitude.

Environmental Satellite estimated hemispheric power was used to drive the NOAA aurora. The activity in the IMF and hemispheric power for this day is shown in Figure 1. The second type of potential patterns used were those estimated by the Super Dual Auroral Radar Network (SuperDARN), which uses HF radar to measure the drift velocity of ionospheric irregularities [*Greenwald et al.*, 1995].

Besides the NOAA auroral model, two additional models were used to specify the aurora. One of these was OVATION Prime [*Newell et al.*, 2010], where auroral precipitation was correlated with measurements of the IMF embedded within the solar wind. The final model used for the aurora was OVATION-SM [*Mitchell et al.*, 2013], hereafter referred to as OVATION-SME or O-SME, which is typically driven by data from the SuperMAG Auroral Electrojet index [*Newell and Gjerloev*, 2011]. In this study, however, data from SuperMAG was unavailable, so O-SME was driven by data from the more widely available Auroral Electrojet index (as of the writing of this paper, SuperMAG has since been extended to include the time frame of this storm). The activity in the AE index for this day is shown in Figure 1.

It should be noted that the electric field and auroral drivers for GITM have significant limitations in the descriptions of specific events. For example:

1. Many of the models used (such as the Weimer potential and the auroral models) are inherently statistical, meaning that they are an empirical representation of the dynamics of the system based on averaged data. Because the average is able to tolerate large deviations, any specific event may look completely different than the statistically modeled mean.
2. The electric potential and auroral models were not derived from the same data sets and do not use the same methodologies. Therefore, any correlation, anticorrelation, or noncorrelation that may or may not exist between the models may or may not represent reality.
3. The resolution of the auroral models and data that are used as drivers is coarser than the actual structure of the aurora. This implies that even though GITM may have the ability to be run with a spatial resolution of 1 km or better, the models driving GITM are still at a coarser resolution, so the dynamics described by GITM would still be at a 100 km or larger-scale size.

In many ways, these limitations reinforce the conclusions of this study which ultimately state that it is difficult to simulate the dynamics of the mesoscale neutral wind patterns in the auroral zone, despite using a wide variety of electric field and auroral precipitation models.

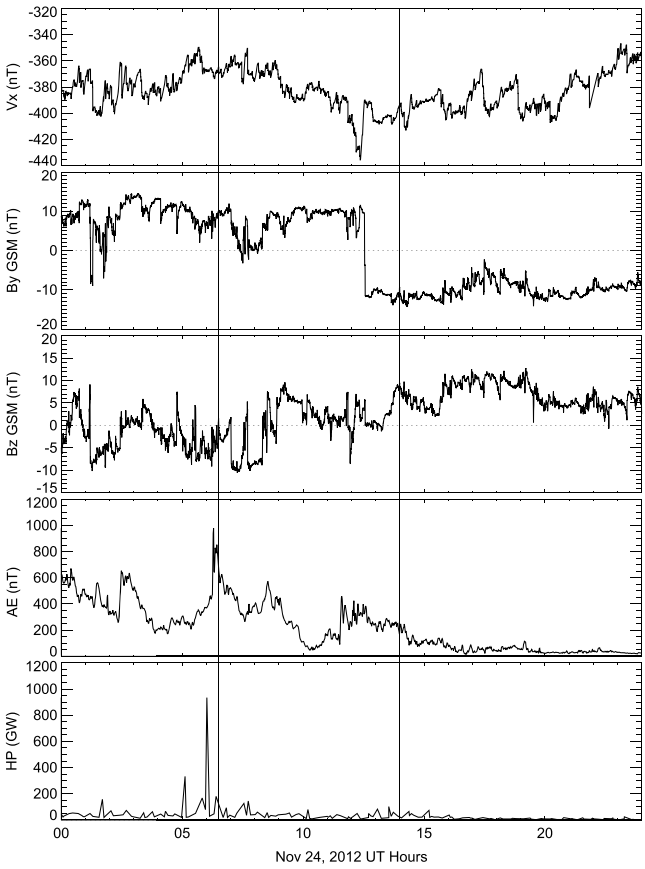

Figure 1. IMF, AE index, and hemispheric power for 24 November 2012. The vertical lines correspond to 06:30 UT and 14:00 UT.

The low-latitude electrodynamics solver within GITM requires a high-latitude boundary condition. This can be treated by using different approaches, but a common method is to set a boundary such that poleward of the boundary, the potential is specified by the high-latitude potential pattern, whereas equatorward of the boundary, the potential is computed self-consistently by the ionospheric neutral wind-driven dynamo solver. Ions were therefore affected differently in runs that used the dynamo and in runs that used a different location of the high-latitude boundary, and the coupling of ions and neutrals resulted in different neutral wind behavior.

With the result from *Deng and Ridley* [2006], an increase in coupling between ion drifts and neutral winds during times of heightened geomagnetic activity is expected. Because that study was an idealized investigation of the coupling, we were interested in understanding the effects that different high-latitude ionospheric drivers can have on the ability of GITM to accurately model neutral winds under "realistic" conditions. To do this, 13 different simulations were carried out, each with different high-latitude drivers: a single driver was chosen to model the ionospheric electric potential, and a single driver was chosen to specify the auroral precipitation at the upper boundary. The ionospheric dynamo was then either turned on or off. Table 1 shows each run performed, along with the models chosen to be used as high-latitude ionospheric drivers, the abbreviation for each individual run, the root-mean-square error (RMSE) and mean difference between winds from each GITM run and observed winds from the Scanning Doppler Imagers (SDIs) deployed throughout Alaska, and the directionally averaged RMSE and difference between GITM simulated and SDI observed temperatures. The east-west (zonal) component of the wind will be presented separately from the north-south (meridional) component, because the ionospheric drivers that influence zonal flows are typically larger than those that dominate meridional flows. The abbreviations found in Table 1 will be used to identify the various runs throughout the remainder of the paper.

2.2. Instrumentation

To validate the simulation results, the GITM computed winds were compared to observed measurements from three Fabry-Perot Scanning Doppler Interferometers (SDIs) located at the Poker Flat (PKR), High-Frequency Active Auroral Research Program (HRP), and Toolik Lake (TLK) research facilities in Alaska (see *Conde and Smith* [1995], *Conde and Smith* [1997], and *Conde and Smith* [1998] for further discussion on the instruments). Each SDI measures line of sight velocities and temperatures of the thermosphere at approximately 240 km altitude. The measurements from the SDIs were compared to GITM. Additionally, electron density data from the Poker Flat Incoherent Scatter Radar (PFISR) located at Poker Flat, Alaska, was compared to the electron density produced by each GITM run. The electron density to the southwest of PFISR was compared, as viewing the density to the north of the instrument would give a less precise description of the substorm because the instrument often observed slight increases in electron density to the north even during quiet times.

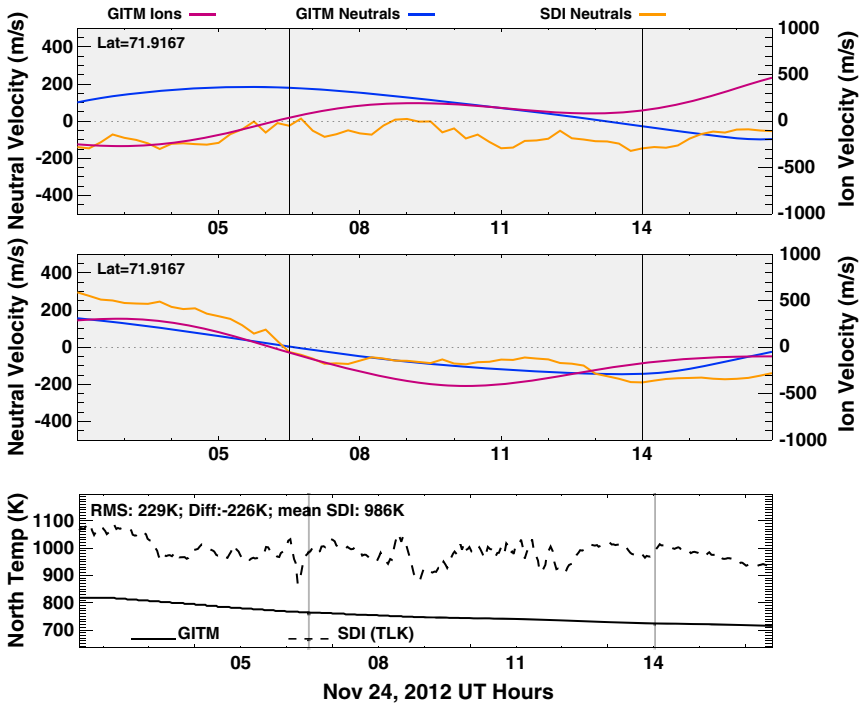

Figure 2. (top and middle) Zonal and meridional flows of GITM computed ions (red) and neutrals (blue), and SDI observed neutrals (orange) at 71.9° latitude. (bottom) Comparison of neutral temperatures at TLK between GITM (solid) and SDI (dashed) for the baseline simulation for the north look direction of the instrument.

3. Results

3.1. Baseline Simulation

For the baseline run, the Weimer potential model was driven with constant IMF values of $B_z = -2.0$ nT, $B_y = 0.0$ nT, and $V_x = -400.0$ km/s, and the NOAA aurora was approximated by constant, extremely low-level (1 GW) auroral precipitation. This simulation was conducted to understand the background wind patterns so that the effect of the electric potential and auroral forcing on the winds could be better understood. The ion flow velocities modeled by GITM in the *F* region were primarily E×B drifts and thus represented the flows driven by the electric potential pattern. The baseline simulation was inaccurate at representing the zonal flow throughout the entire night as demonstrated by Table 1.

Figure 2 shows the GITM simulated and SDI measured zonal and meridional winds and thermospheric temperature at a fixed latitude (71.9°) throughout the night. Significant differences exist between observed and modeled results. These are primarily caused by the fixed and weak electric field and auroral precipitation patterns used. Clearly, the baseline simulation is much better at replicating the observed meridional neutral flow patterns than the observed zonal neutral flow patterns. Figure 3 gives a more global perspective on why such a disagreement exists. This Figure shows the modeled zonal (left) and meridional (right) neutral winds as color contours along with ion flow velocities as vectors for the baseline run at 06:30 UT. The field of view for each SDI array is also plotted, centered around the location of each instrument. In this run, the neutral wind flows suggest a very general motion from the dayside to the nightside. The zonal flows show a divergence of the wind at noon and a convergence in the predawn region. These winds do not agree well with the ion flows at high latitudes: neutrals flow eastward where ions stream westward, especially over the SDI instruments. In general, there is no structure in the wind that suggests any type of dynamic behavior in the atmospheric transport. Because of the lack of auroral precipitation throughout the night, there appeared to be little to no coupling between the neutrals and ions—not simply over Alaska, but throughout the entire high-latitude region—and is reflected in the amount of error seen in this run in Table 1. Figure 3 (right) shows that at 06:30 UT the meridional flow of the neutral winds was predominantly poleward on the warm side of the polar cap and equatorward on the cool side. This behavior continues throughout the entire event in this run and demonstrates that neutral wind patterns align with thermal and pressure gradients without substantial ionospheric forcing.

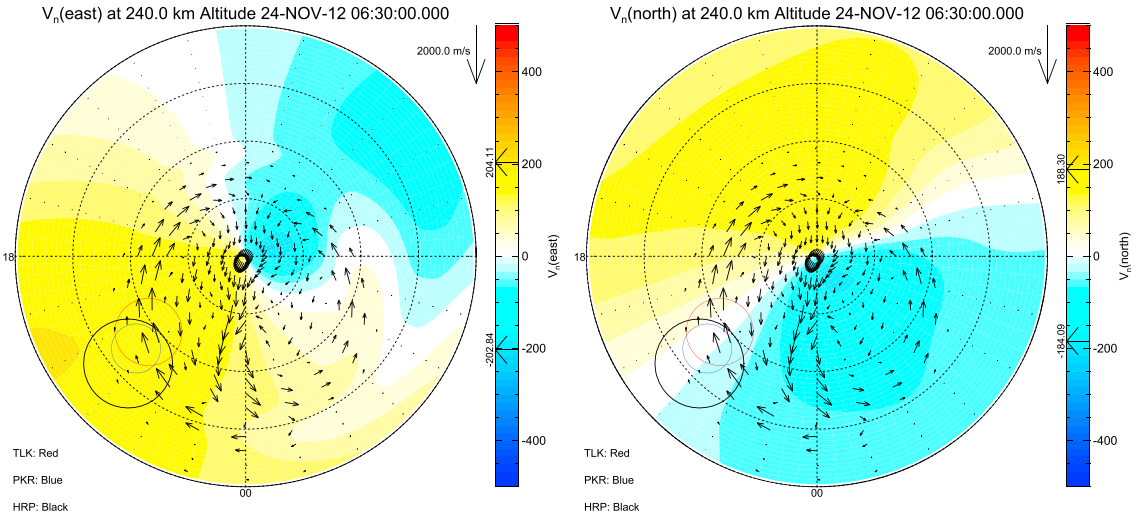

Figure 3. (left) Zonal and (right) meridional flow directions for the baseline run at 06:30 UT. Reds and yellows indicate eastward or northward flowing neutrals and blues indicate westward or southward flowing neutrals. The plot is overlain with ion flow vectors.

One of the leading causes of heating in the high-latitude ionosphere is Joule (frictional) heating (see, for example, *Foster et al.* [1983] for frictional/Joule heating at high latitudes and *Deng and Ridley* [2007] for Joule heating in global models). Joule heating is strongest in the presence of both increased electric fields and increased particle precipitation. Therefore, during times of heightened geomagnetic activity, an increase in ionization rates and electric fields in the high-latitude region causes an increase in the frictional heating between the ion and neutral particle populations, creating a net atmospheric temperature increase. Because GITM modeled little change in electric field and precipitation for the baseline simulation, the temperature steadily decreased throughout the night in this run (see Figure 2, bottom). Further, little variation of the temperature in addition to this steady decrease was observed. This simulation was a poor representation of the actual temperature structure throughout the night because there was no dynamic electron precipitation to drive thermospheric heating.

3.2. Weimer NOAA Simulation

Figure 4 shows the ion and neutral flows and electron precipitation simulated and observed over the SDIs throughout the night for the WN simulation. Plotted in orange are the observed neutral winds from SDI, in blue are the simulated neutral winds from GITM, and in red are GITM simulated ion flows. In this case, the wind data were derived by combining all of the line of sight SDI data from the three instruments to create two-dimensional vectors over the measurement area. The process of converting line of sight data to vector flows using monostatic and bistatic (or tristatic) techniques is described in *Conde and Smith* [1997] and *Anderson et al.* [2012], respectively. The velocities were averaged zonally to provide a temporal history of the winds along a single meridional slice. The GITM data were derived by taking a single meridional slice through the model at the averaged longitude and linearly interpolated between the model output files to the measurement times. Lines are drawn at 06:30 and 14:00 UT for reference to the 2 times that are explored more closely throughout this study, as described below. Finally, electron density from the model at approximately 240 km altitude and at $\pm 1^\circ$ from the center latitude is contoured under the winds and used as a proxy for the amount of ion-neutral coupling that may occur. The changes in density between the simulations are useful in comparing the effect of using different auroral precipitation models and allow for an idea of how effectively the auroral model captures the precipitation during the substorm.

While the baseline run had no electron precipitation due to the constant drivers in the auroral precipitation model used, the WN simulation created large amounts of electron density throughout the night. The electron density increase also created much more ion-neutral coupling in the modeled flow, which allowed for a more accurate representation of the zonal neutral wind flow structure over the SDIs, as the simulated GITM neutral flows matched the observed SDI flows throughout most of the night (Figure 4, left). The WN simulation showed much better agreement between the ion and neutral flows in the high-latitude region compared to the baseline run. The meridional flows in Figure 4 (right) show significant ion-neutral coupling

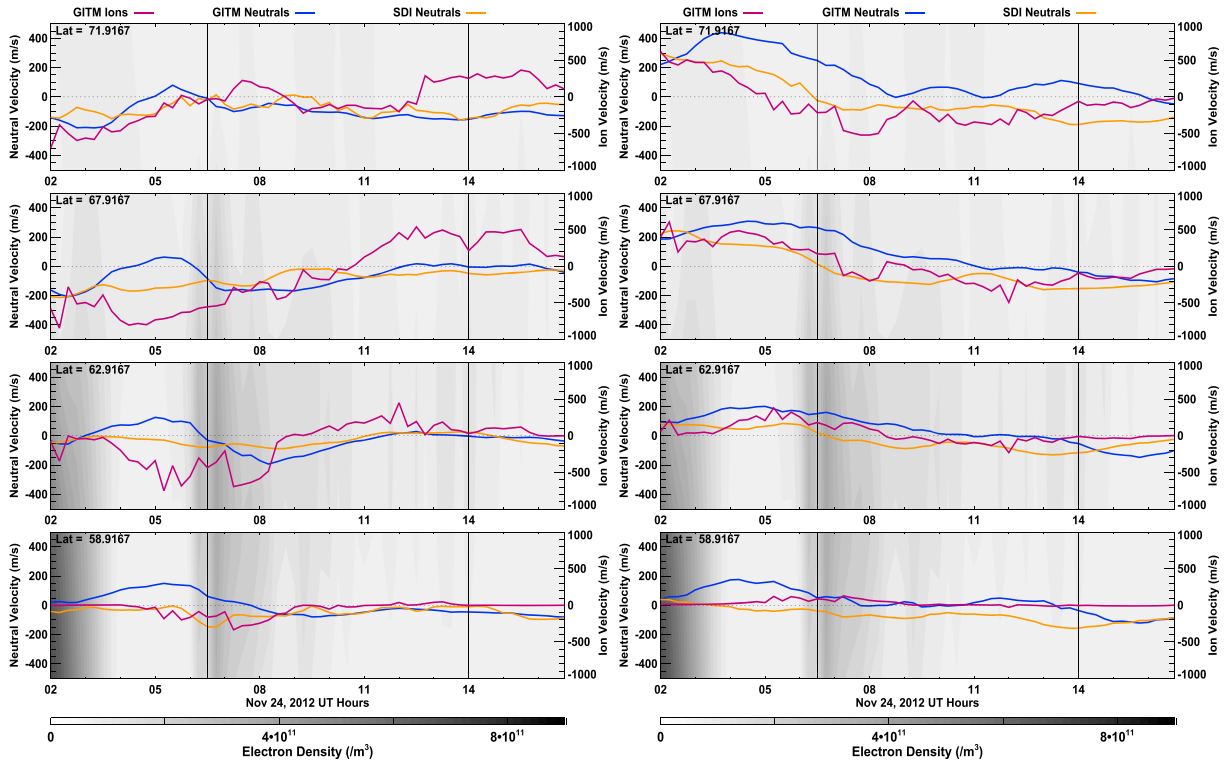

Figure 4. Selected (left) zonal and (right) meridional neutral and ion flows for the WN run at various latitudes. In orange is the measured neutral wind that is observed by SDI at a given time, and in blue is the neutral wind simulated by GITM. The red line shows the flow of the ion species modeled by GITM. The vertical black lines indicate the 2 times examined in the study, 06:30 and 14:00 UT. Contoured beneath the flows is the GITM electron density, a proxy for auroral intensity, at ±1° from the denoted latitude.

as well. Although the flows of the two constituents are not identical, the influence that the ions have on the neutrals is obvious, especially at lower latitudes where the GITM results agree well with the observed SDI meridional flows. However, at higher latitudes, the GITM neutral flows differ significantly from the SDI flows. These differences may be driven by an area of heating within GITM causing a north-south divergence in the flow between 68° and 72° latitude toward the end of the night.

To better understand any local time dependence in the model on producing neutral winds, two individual time periods were considered, 06:30 UT and 14:00 UT, which correspond to approximately 20:40 and 04:10 local time (LT) in Alaska. These times ensure that any electron density seen in the GITM simulations over Alaska was a result of auroral precipitation and not ionization from the Sun. The choice of these 2 times also corresponds to a significant increase in electron density modeled by multiple GITM runs for this day. This increase was observed to begin around 06:30 UT, and either end or slightly reintensify near 14:00 UT, depending on which drivers were used. Focusing on these 2 times allowed for a direct comparison of the similarities and differences in the winds and electron densities between simulation results with various high-latitude drivers during the substorm event. Figure 5 shows that in the zonal flows at 06:30 UT, the ions and neutrals were highly coupled over the SDIs (much more than in the baseline simulation), as evidenced by the westward ion and neutral flows in the premidnight region. Near 70° in the postmidnight region as well, the east-west ion and neutral flows were in the same direction. At 14:00 UT however (Figure 5, top right), while there was still substantial ion-neutral coupling near local noon and local dusk, the simulated neutral and ion flows were less coupled over the SDIs. The neutral flow was mainly westward, whereas the ion flow was eastward throughout the three SDI fields of view, caused by the reduction in electron density modeled at this time. Despite this, the simulated GITM zonal winds better matched the SDI zonal winds at this later time.

Even though the zonal flow patterns simulated in the run with WN drivers agreed with the observed SDI flow patterns, the meridional flows did not match as well. In general, the global wind pattern of the thermosphere is such that the neutrals flow from the dayside of the planet to the nightside, in accordance with the

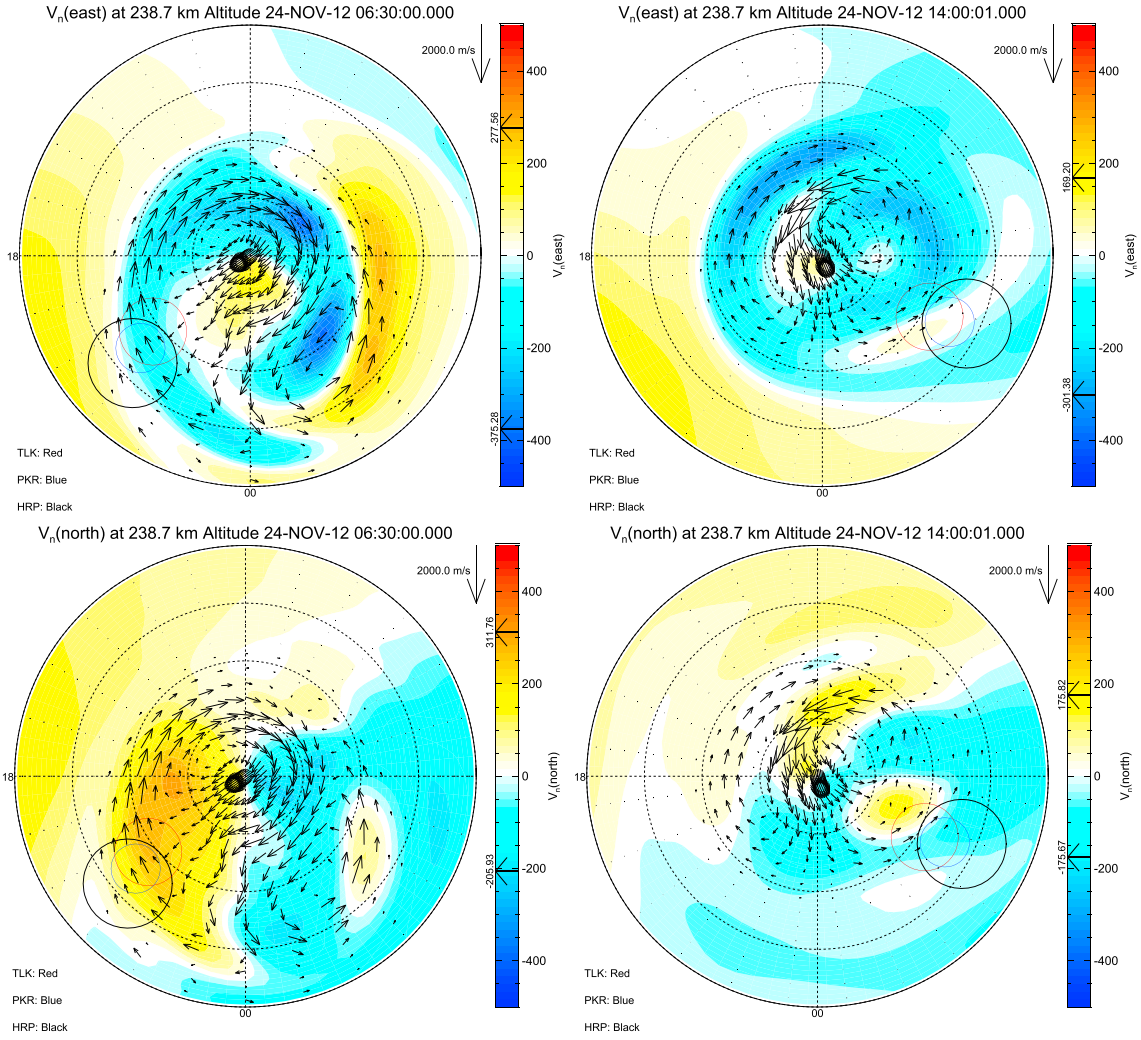

Figure 5. Similar to Figure 3 but for the WN simulation, with (top) zonal and (bottom) meridional flows at (left) 06:30 UT and (right) 14:00 UT.

thermal gradient between the two hemispheres. For the meridional component, this means that the flow should be close to zero near dusk (04:00 UT) and dawn (16:00 UT), and equatorward on the nightside, which is what was roughly observed in the baseline run and in the SDI data, as shown in Figure 2 (middle). Thus, at 02:00 UT (predusk) if the flow were from the dayside to the nightside, the observed winds should have been slightly poleward, which the SDI winds indicated. As Alaska moved through dusk, the meridional flow should have gone to zero and then become equatorward thereafter. This occurred closer to 06:30 UT in the SDI data and much later (if at all) in the GITM results. The flow should have then returned back toward zero near dawn. Figure 5 (bottom) shows that at 06:30 UT, the structure of the meridional flow in the neutrals was rotated by approximately 90° (above 60° latitude) from the day-to-night flow observed in the baseline simulation. Instead of flows across the terminator, the flow was across the noon-midnight plane. This disagrees with the winds measured by the SDIs and also disagrees with the simple pressure gradient force mechanism. At 14:00 UT, the neutrals follow the pressure gradient better than at 06:30 UT, but the simulated GITM neutrals disagreed with the observed SDI neutrals. Because the WN simulation may overly couple the ions with the neutrals, the meridional neutral flow patterns were less accurate in this run than in the baseline run. This is clearly demonstrated in Table 1, as the WN simulation was the least accurate in modeling meridional flows.

With the active precipitation shown in Figure 4, the ability of GITM to model the dynamics of the electron density above PFISR was studied. Figure 6 (left) compares the electron density modeled by GITM and observed by PFISR as a function of altitude and time. Additionally, the total electron content (TEC), an integral of the electron density with altitude, is plotted for each. The increases in electron density near 06:00 UT

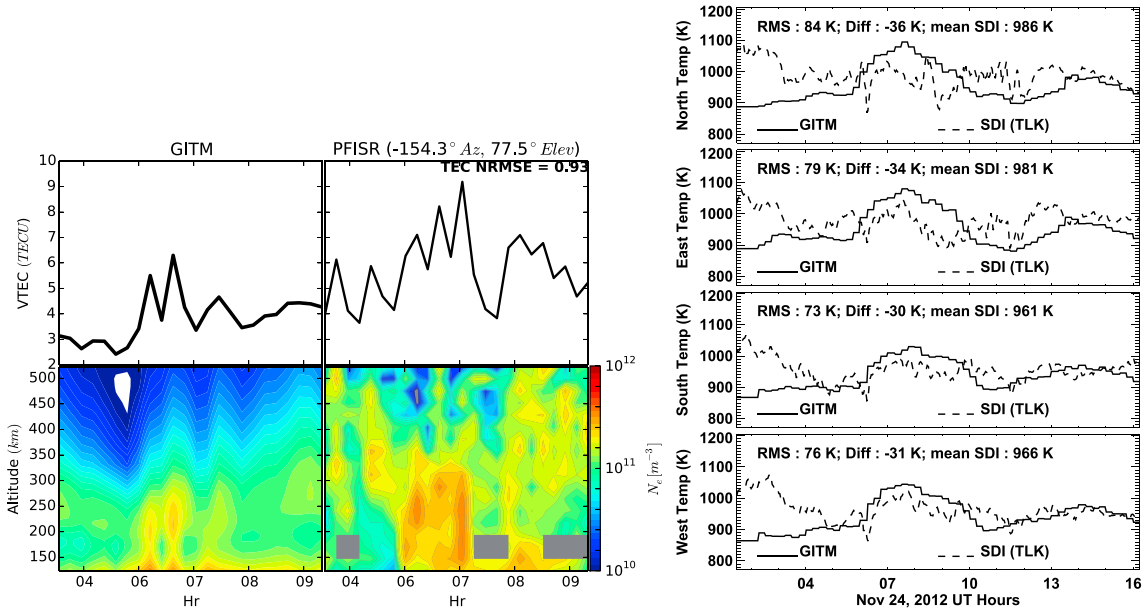

Figure 6. (left) GITM and PFISR electron density and TEC data for the WN run. The normalized root-mean-square error in the TEC is shown between GITM and PFISR, along with the PFISR look direction. (right) Similar to the temperature portion of Figure 2 but for the WN simulation. In addition to the north look direction plotted first, from the second panel to the bottom are the east, south, and west look directions of the instrument.

were captured by the WN simulation but did not last long enough. Whereas the observed density increase was sustained for more than an hour with two large peaks in density during this time, the simulated density only captured two sudden increases in density. In addition, the modeled precipitation did not cause enough ionization at high altitudes.

Because of the increase in auroral precipitation and electron density shown in Figures 4 and 6 at multiple times throughout the night, it is expected that these times should be marked by an increase in Joule heating and thus an increase in the temperature of the neutral atmosphere. Figure 6 (right) shows temperatures measured by the SDI instruments at TLK and modeled by GITM, along with the root-mean-square error and absolute difference between the two for the WN run. Near 06:30 UT, when GITM modeled a substorm onset and an increase in electron precipitation, a temperature increase was simulated in all look directions around the SDI. Even though this increase was too large, the structure of the change in temperature was well matched. A slight temperature increase was modeled over the TLK instrument at 14:00 UT as well, but to a much lesser degree than the increase at 06:30 UT.

3.3. Weimer OVATION-SME Simulation

In comparison to the WN run, the WOs run created different behaviors throughout the night as demonstrated in Figure 7. Where WN had very sudden electron precipitation increases that extended to latitudes lower than 57° at 06:30 UT and sporadic precipitation throughout the remainder of the night, the precipitation in the WOs simulation built up more gradually before the large increases in density occurred. These precipitation events did not reach latitudes that were as low compared to the WN simulation but created more electron density in the high latitude regions. The increase in electron density was a direct result of changing only the auroral pattern driving the model, as the same high-latitude imposed electric potential pattern [*Weimer*, 2005] was used. Despite the slight differences in precipitation, the east-west neutral flows were alike in both of the simulations, as quantified in Table 1. However, an increase in accuracy between the two simulations was observed near 06:30 and 14:00 UT where GITM simulated more electron precipitation with the O-SME aurora. In addition, at high latitudes, the modeled and observed zonal flows were in much better agreement in this simulation. Although at lower latitudes between 04:00 and 06:00 UT the GITM winds became eastward while the SDI winds were westward, after this time the modeled zonal flows were closer to the observed zonal flows.

In the high-latitude region of the WOs simulation, the ions and neutrals almost always flowed in the same direction and the neutral winds in GITM were often larger than SDI winds where this occurred, especially in

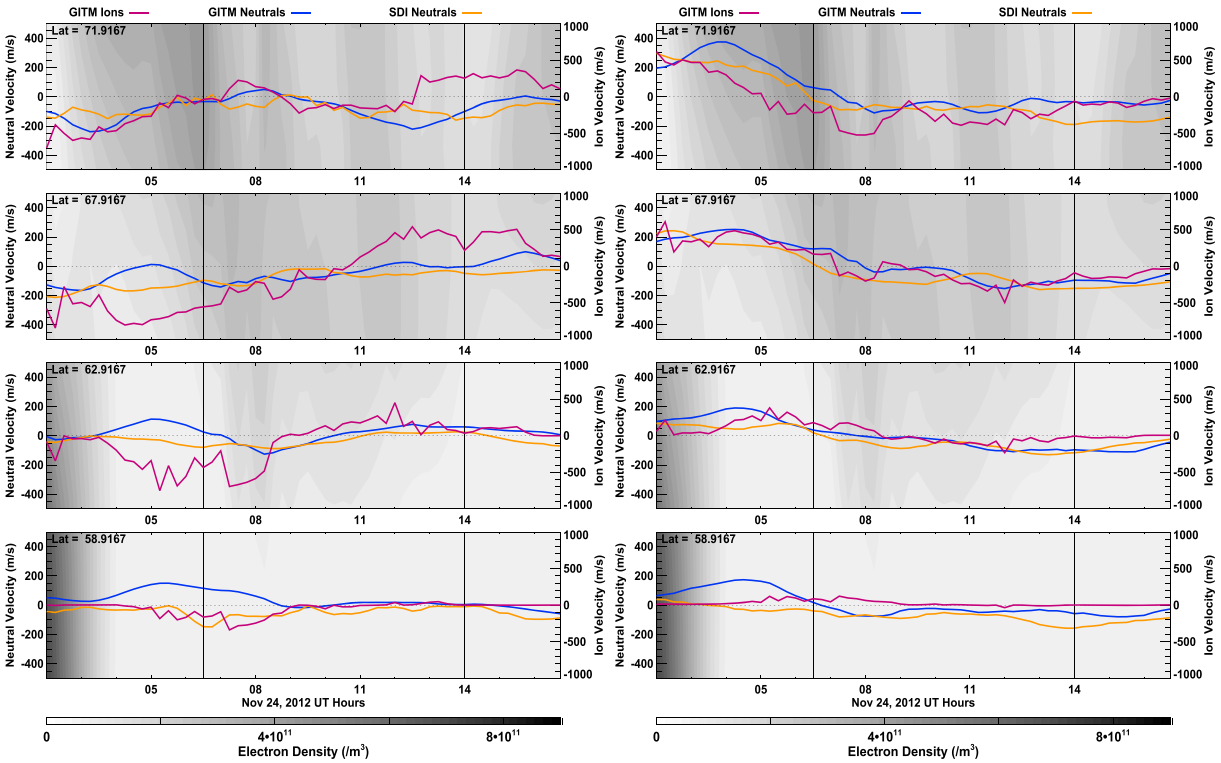

Figure 7. Same as Figure 4 but for the WOs run.

the meridional flows. In the study presented by *Deng and Ridley* [2006], a similar behavior was seen. They conclude that when the ion drag and gradient in pressure forces in the high-latitude region are in the same direction, a large and often sustained neutral wind velocity can be observed. The meridional neutral winds demonstrated this behavior for the WOs simulation and is clear in Figure 7. Early in the night, where GITM modeled northward flow in the high-latitude region, the winds were much larger than the SDI winds at this time. This behavior is not only seen in the north-south flow in the WOs simulation but also in some of the other simulated meridional flows with different high-latitude drivers. Therefore, the runs that have less intense auroral activity and less active electric potential patterns—leading to weaker ion flows—tend to be more accurate in modeling meridional behaviors. For this reason, the WOs run was not as accurate in modeling the meridional neutral flow patterns as the baseline simulation.

Using the same electric potential, the WOs run had nearly identical ion flows as the WN run and the structure of the zonal neutrals was similar as well. However, a major difference between the two simulations is revealed by comparing Figure 8 with Figure 5. The strength of the westward flow of neutrals extending from approximately 02:00 LT through dusk to 10:00 LT, accompanied by an eastward jet beginning around 02:00 LT and extending through dawn to converge with the westward winds near 10:00 LT, had a larger magnitude in the WOs simulation. These neutral winds correspond nearly identically to the ion flow patterns modeled in the WOs case, representing a stronger coupling of the ions and neutrals. This is true both at 06:30 UT and 14:00 UT, as well as in the zonal and meridional directions. There were differences between the ion and neutral flows, however. For example, at 06:30 UT near the SDIs, the ions were exclusively westward, while the neutrals exhibited a shift from westward flows at high latitudes to eastward flows at low latitudes. The WOs simulation had a more accurate representation of the zonal neutral winds than the baseline run. As described above, prior to 14:00 UT (but after 06:00 UT), the GITM flows agreed with the SDI flows (see Figure 7). The flows then began to disagree after 14:00 UT, when the amount of ion-neutral coupling within the simulation increased.

There were multiple differences between the WN and WOs simulations in the meridional flow of neutral winds as well. The WOs run was a better representation of the north-south flow across the terminator when compared with the SDI data. At 06:30 and 14:00 UT, the neutral flow patterns in the WOs simulation

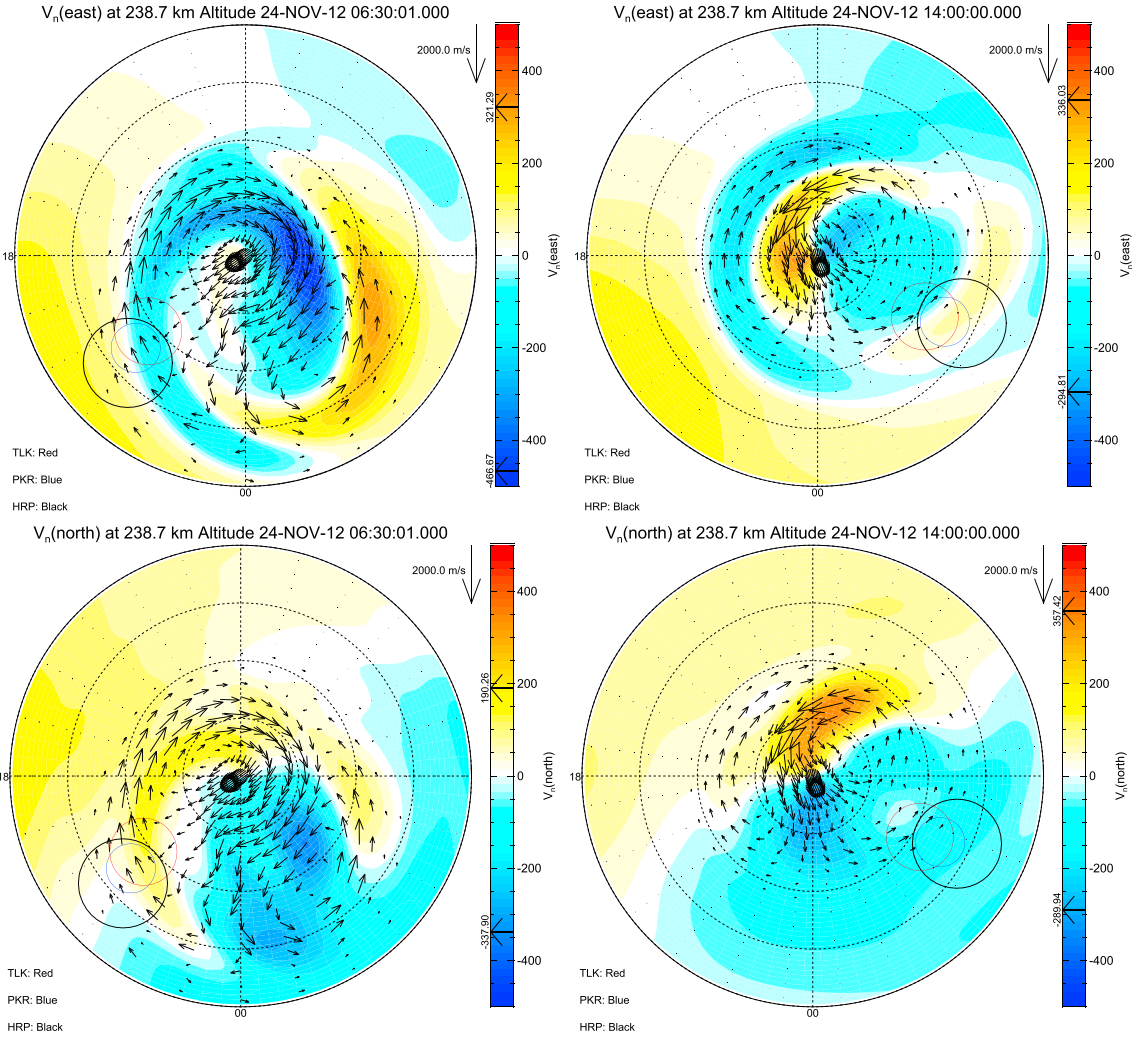

Figure 8. Same as Figure 5 but for the WOs run.

were more north-south than in the WN simulation and were more similar to the SDI flows. In addition, the strong northward flow that extended to postdusk at 06:30 UT was gone by 14:00 UT, suggesting that the flow pattern was driven strongly by the amount of electron density in the model, as there was a large decrease in electron density between 06:30 UT and 14:00 UT. The behavior at 14:00 UT was similar to what was observed in the baseline run throughout the entire night. With less electron density, the neutral winds flowed in a meridional direction following the gradient in pressure. The modeled winds showed slightly better agreement with the observed winds at 14:00 UT than at 06:30 UT because of this decrease in electron density.

In comparing electron density data from PFISR with simulated density from the WOs run in Figure 9 (left), it is clear that near 06:00 UT, both PFISR and GITM showed an increase in auroral precipitation; however, the electron density modeled by GITM did not extend to low enough altitudes. In addition, the buildup of the electron density in the model was more gradual than the sudden spike that was observed by PFISR. Whereas PFISR measured a slight increase in density around 05:45 UT and a sudden increase just after 06:00 UT, GITM modeled an increase starting around 05:45 UT and continuing until 07:00 UT, where a distinct peak occurred. After 08:00 UT, where PFISR measured only a slight increase in electron density at low altitudes, GITM simulated a second increase in electron density similar to the peak modeled around 07:00 UT.

Figure 9 (right) is similar to Figure 6 (right) but with OVATION-SME specifying the auroral precipitation as opposed to the NOAA method. With these drivers, the dynamic electron density throughout the night yielded less of a temperature change during the times of increased electron precipitation but showed

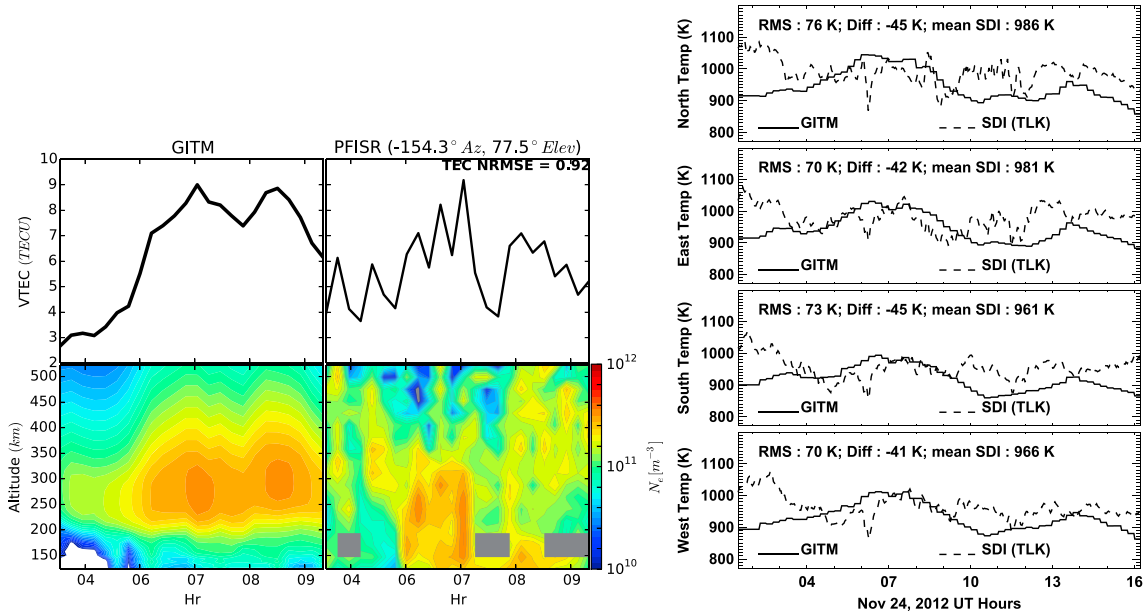

Figure 9. GITM and PFISR electron density and TEC data and GITM and TLK thermospheric temperature for WOs, in the same format as Figure 6.

fluctuations in temperature that were closer to the observed temperatures from the instruments. Near 06:30 UT where there was a large increase in electron density in the simulation results, there was a temperature increase in all look directions at this time, driven by Joule heating in the simulation. A similar temperature increase was also simulated at 14:00 UT. Further, the overall temperature was slightly lower in GITM driven by OVATION-SME compared to GITM driven by NOAA aurora, although both were similar in reproducing the temperature as seen by comparing the temperature errors between the two runs in Table 1.

3.4. SuperDARN OVATION-SME Simulation

Figure 10 shows the results of GITM when SuperDARN potential patterns and OVATION-SME aurora were used. With this electric potential, the ion flows were much more dynamic and intense, which drastically affected the neutral winds. From 08:00 to 10:00 UT and around 63° latitude, GITM modeled the most intense westward flows of neutrals and ions compared to any other run. While GITM overestimated the observed winds, the ions and neutrals were heavily coupled with one another. In comparing the WOs and SdOs runs, a surprising difference between the two is the electron density at 240 km. SdOs showed the same spikes in electron density at 06:30 and 08:45 UT, but they were more spread out than in the WOs model. In addition, this model showed two further electron density intensifications located at times just before 14:00 and 16:00 UT, after previously modeling decreases in density. These differences are caused by the fact that at 240 km, advection can strongly control the electron density as well as the precipitation pattern. The behavior described above demonstrates the strong need for an accurate representation of both electric potential and electron precipitation patterns within the simulation.

At 06:30 UT, the zonal winds simulated in this case were weaker than the zonal winds simulated by WOs. For example, Figure 11 (top) shows that the strong premidnight westward flow of neutrals was no longer present in this run, and the postmidnight eastward flow of neutrals was slower by approximately 160 m/s. Clearly, the electric potential pattern chosen dramatically affected the neutral wind patterns. Despite the additional increase in electron density at 14:00 UT, the zonal winds for the SdOs run shown in Figure 11 (top right) were weaker than the simulation by WOs. This was mostly due to the weaker ion flows specified by the SuperDARN potentials. However, at the location of the SDI instruments, these drivers allowed the model to replicate the observed neutral winds well.

In the meridional direction, as with the WN and WOs runs, the SdOs run overly couples the ions and neutrals. As described above, where the ions and neutrals flowed in the same direction, the neutral flows became too large. This is seen in Figure 10 (right) between 03:00 and 07:00 UT, where the high-latitude neutral winds were too large in comparison to the SDI winds by nearly 100 m/s. Because of this, the meridional flows for this run were much less accurate than in the baseline simulation. In addition, the increase in electron

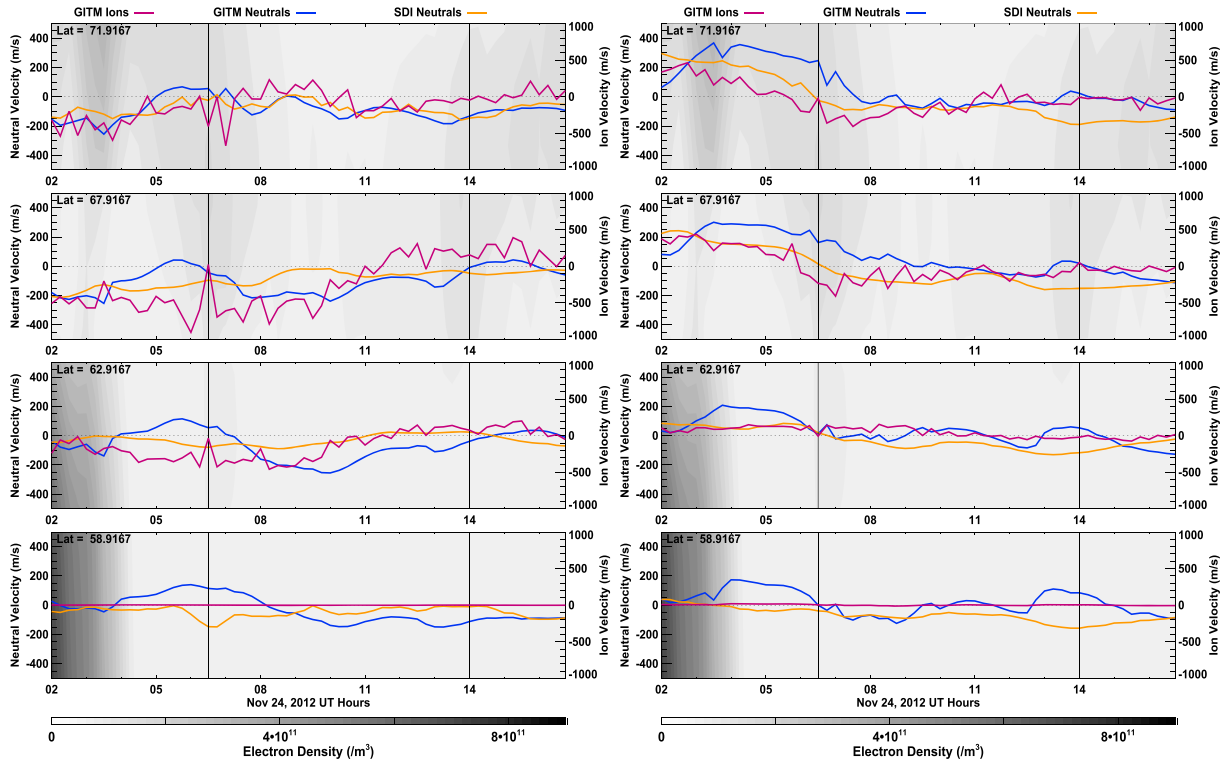

Figure 10. Same as Figure 4 but for the SdOs simulation.

density around 14:00 UT created ion-neutral coupling that prevented the accurate modeling of the winds—the neutrals followed the ions more than the gradient in pressure. Figure 11 (bottom right) shows that the modeled meridional winds did not follow the expected pattern of the meridional neutral flows and were not representative of the winds observed by SDI because of the coupling.

Figure 12 (left) shows the modeled and observed electron density and TEC for the SdOs simulation. Two electron density increases at 06:30 and 08:45 UT were visible in the GITM results. While the density was similar at lower altitudes between the WOs and SdOs runs, above approximately 200 km the two runs differed substantially, although both simulations modeled an additional increase in electron density near 08:00 UT that was not observed by PFISR. As was visible in Figures 10 and 12, the profile of the electron density in the SdOs simulation was more structured and dynamic than most other runs, and created a slightly lower density than the WOs run.

Simplistically, with less electron density in the model, it would be expected that the amount of Joule heating in the SdOs simulation and the atmospheric temperature increases near 06:30 and 14:00 UT would be less than in the WOs simulation. However, this was not the case. For the SdOs drivers, Figure 12 (right) shows that the neutral temperature modeled by GITM to the north and east of the TLK instrument was much higher than the modeled temperature in both the WN and WOs runs. This occurred because in the location of the SDI instruments, the momentum of the ions and neutrals was not coupled as well here as they were in other model runs. Because the ions and neutrals flowed in opposite directions from one another, the difference between the two flows caused stronger Joule heating. Therefore, a significantly larger temperature increase in this simulation was observed. This temperature increase did not agree with what was observed by the SDIs, however, as an increase in RMSE between the GITM and SDI temperatures was observed compared to the WN and WOs simulations (see Table 1). Interestingly, there was a larger temperature gradient in the GITM results for this run than for any of the other runs. For example, at the peak temperature in the northward direction, the southward direction simulated temperatures that were 100 K lower. This highlights the importance of having an auroral model that has relatively fine spatial scales.

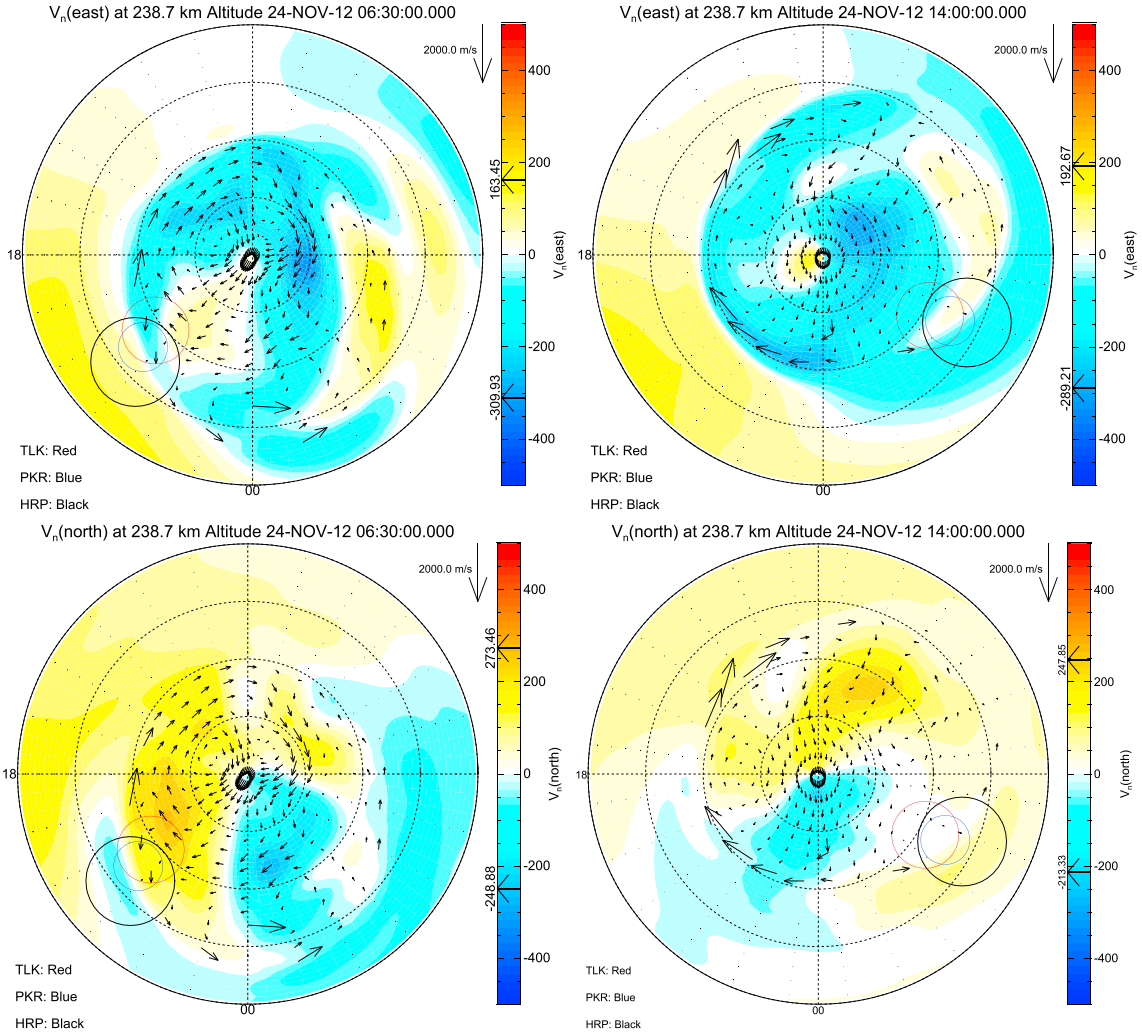

Figure 11. Same as Figure 5 but for the SdOs run.

3.5. SuperDARN OVATION Prime Simulation

Figure 13 shows similar parameters as Figures 4, 7, and 10 but for the SdOp simulation. While the neutral winds for both runs with SuperDARN potentials show similarities, the electron precipitation was significantly different. The SdOp simulation specified much less auroral precipitation than the simulations driven by OVATION-SME. Compared to the SdOs simulation, SdOp had meridional neutral flows that were closer to the observed SDI flows. In Figure 13, it is clear that one of the reasons for the increased accuracy is because the northward flow at the beginning of the night was not as large as it was in the SdOs run. This led to the slight increase in accuracy that was seen in the errors for the simulated meridional flows in this run.

The lack of change in precipitation in this simulation is evident in Figure 14 (left). Unlike the three previous simulations, there was no increase in auroral precipitation modeled in the SdOp run. The TEC modeled by GITM was nearly constant with only a small amount of precipitation. Figure 14 (right) shows that the temperature was weaker than in other models with more moderate auroral activity. However, despite the lower modeled temperatures compared to the observed temperatures, the SdOp run still had more fluctuations in the temperature than would be expected from a simulation with no auroral activity or constant potential patterns, indicating the existence of more variability in the electric field coupled with somewhat stronger precipitation than was represented by the baseline simulation. For example, there is a marked temperature increase around 13:30 UT modeled by GITM, suggesting that Joule heating occurred in the model regardless of the fact that less precipitation was present within the run.

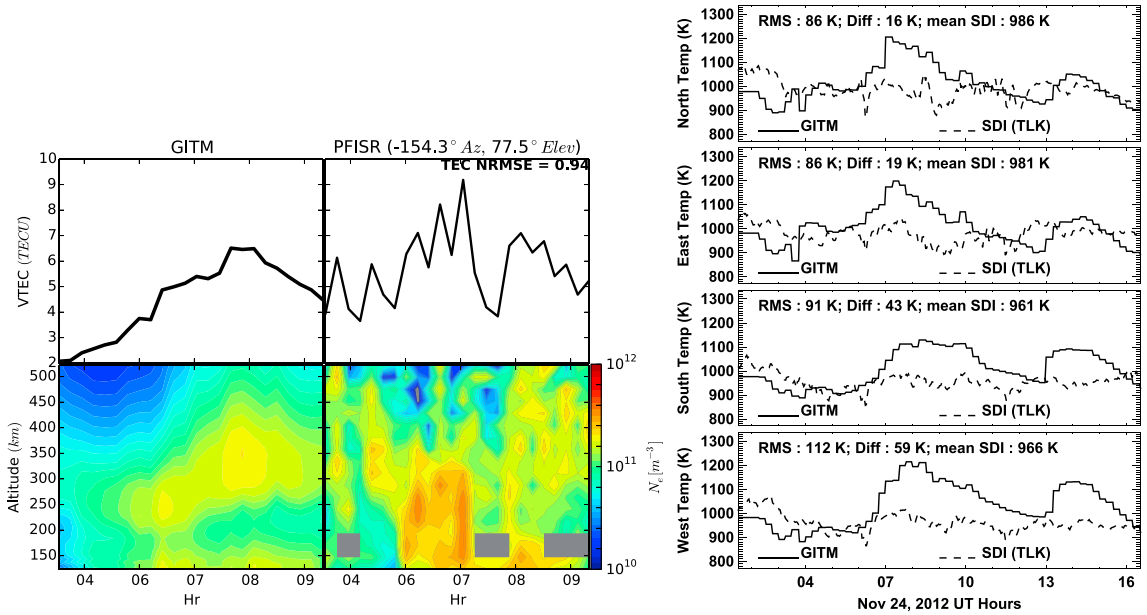

Figure 12. GITM and PFISR electron density and TEC data for SdOs, and GITM and TLK thermospheric temperature in the same format as Figure 6.

3.6. Influence of the Ionospheric Dynamo

The dynamo region has a significant influence on ionospheric dynamics at low latitudes. Modeling this region correctly is therefore important to the understanding of the impact of the dynamo. One of the important features of simulating the dynamo correctly includes understanding the penetration of electric fields from high latitudes to low latitudes. In order to achieve the penetration electric fields, the high-latitude boundary needs to be placed just poleward of the zero potential assumed in all statistical (and some fitted) models of the potential patterns. If this boundary is chosen incorrectly and placed at latitudes that are too high, the winds can act to shield the potential in much the same way that the Region 2 currents shield the potential in reality. If this is done (in a physical way), the winds can be dramatically affected around the boundary of the potential solver. To highlight the importance of the correct placement of the boundary, the SdOsD run is presented. In this simulation, the high-latitude boundary of the solver was placed at 70° magnetic latitude, which was too high. Figure 15 shows similar model parameters as Figures 10 and 11 but with the dynamo turned on. In comparing this run with SdOs in the east-west direction at 06:30 UT (the bottom left image in the figure), it is clear that the resulting ion and neutral flow patterns were significantly different and the overall magnitude of the neutral winds were increased for the model run with the dynamo on. Near the high-latitude region, especially between 70° and 75°, the dynamo completely reversed the direction of the neutral wind flow compared to the run without the dynamo. In the predusk sector where the dynamo region had the strongest effect, the neutral flow influenced by the dynamo cut off the high-latitude ion and neutral flow pattern driven by the SuperDARN potentials. When the SDI instruments were located in the postdusk region at 06:30 UT, a neutral wind that was too strong was modeled by GITM at these locations. This was a direct effect of the intense eastward flows driven by the dynamo. In the meridional winds as seen in Figure 15 (bottom right), the dynamo had less of an effect on the neutral flows. The flows were different in the run that included a dynamo (for example, predawn at 06:30 UT showed slightly more intense flows), but there were no complete flow reversals as there were in the zonal flows.

Figure 15 (top) shows the observed zonal neutral winds and modeled neutral and ion flows for the SdOsD run. As seen in the lower portion of the figure, the region most obviously affected by the dynamo was approximately between 14:00 and 20:00 local time in the east-west direction. As expected, GITM significantly overestimated the strength of the eastward winds between 02:00 and 07:00 UT for all of the runs that included a dynamo with the boundary placed at 70° geomagnetic latitude, especially between 60° and 70° geographic latitude. This is because Alaska passed through a region that was still strongly affected by the dynamo during this time. After 07:00 UT, the overestimation began to decrease, and GITM

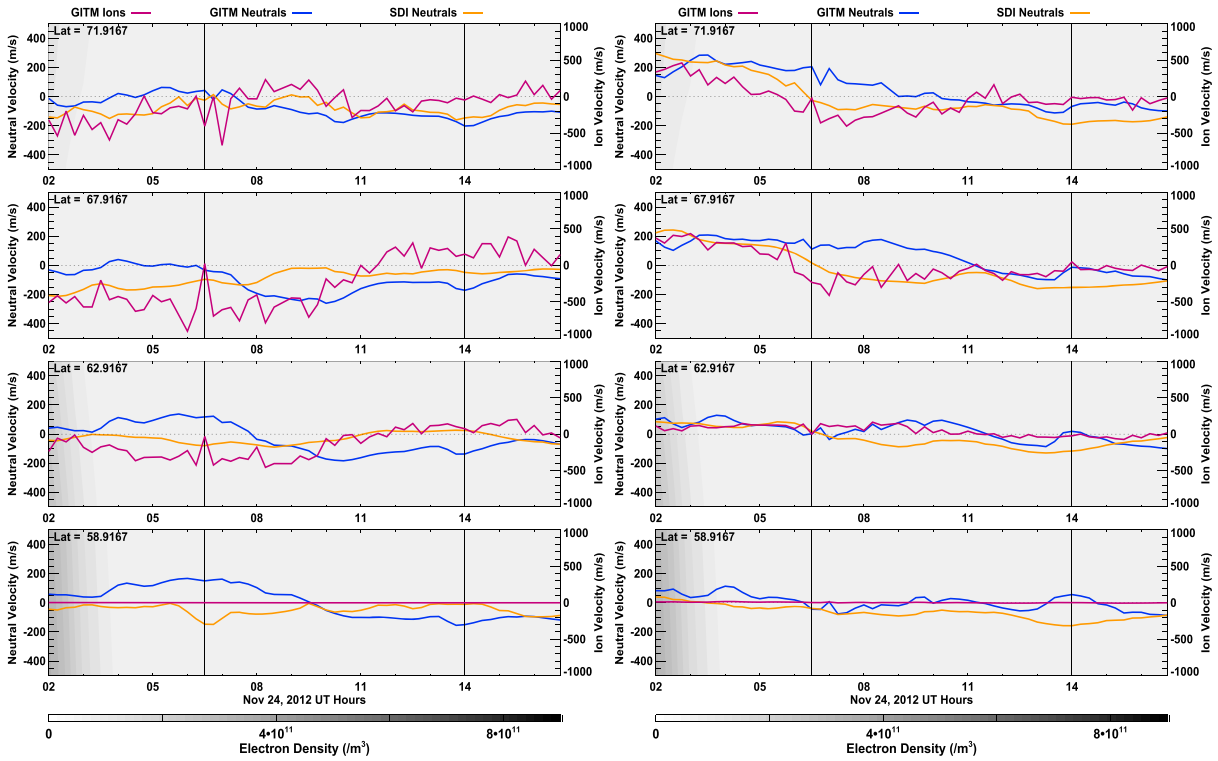

Figure 13. Same as Figure 4 but for the SdOp run.

was better at representing the SDI winds throughout the remainder of the night, since the strength of the eastward neutral winds began to decrease. In the SdOs run, i.e. the run without a dynamo, GITM was better at representing the neutral winds.

The behavior described above occurred in all of the runs with a dynamo located at 70° latitude. Because of the overestimation of the winds, the resulting east-west errors in each run with a dynamo (WND, WOsD, SdOsD, and SdOpD) were significantly worse than the matching run without a dynamo (WN, WOs, SdOs, and SdOp), as demonstrated in Table 1. In the zonal direction, for each group of runs with and without a dynamo, the RMS and difference errors between GITM and SDI were always larger for the run that used a dynamo.

This behavior was simulated in runs with a dynamo located at 50° latitude as well, although to much a lesser degree. With the location of the dynamo moved to lower latitudes, GITM was able to represent the high-latitude zonal neutral winds more accurately since they were not affected by a dynamo in the immediate vicinity. Comparing simulations with a dynamo at 50° and 70°, the runs with a dynamo at lower latitudes were better at simulating the observed winds, as shown in Table 1. Although the mean difference in the zonal flow was lower in the SdOpD simulation compared to the SdOpD50 simulation, this was because the GITM winds were more extreme in opposite directions and brought the difference closer to zero. The only exception where a simulation using the dynamo provided more accurate zonal flows was the SdOsD50 run. In the north-south direction, there appeared to be less of an effect of the dynamo because the flows driven by the dynamo at higher latitudes were generally zonal as opposed to meridional.

4. Discussion

The modeling of neutral winds in the high-latitude region is significantly dependent on the drivers used within each simulation. Table 1 demonstrates this as models with even slightly differing drivers can be substantially dissimilar from one another. However, at auroral latitudes, these drivers have more of an effect on zonal neutral winds than on meridional neutral winds. Overall, the north-south errors were less than the

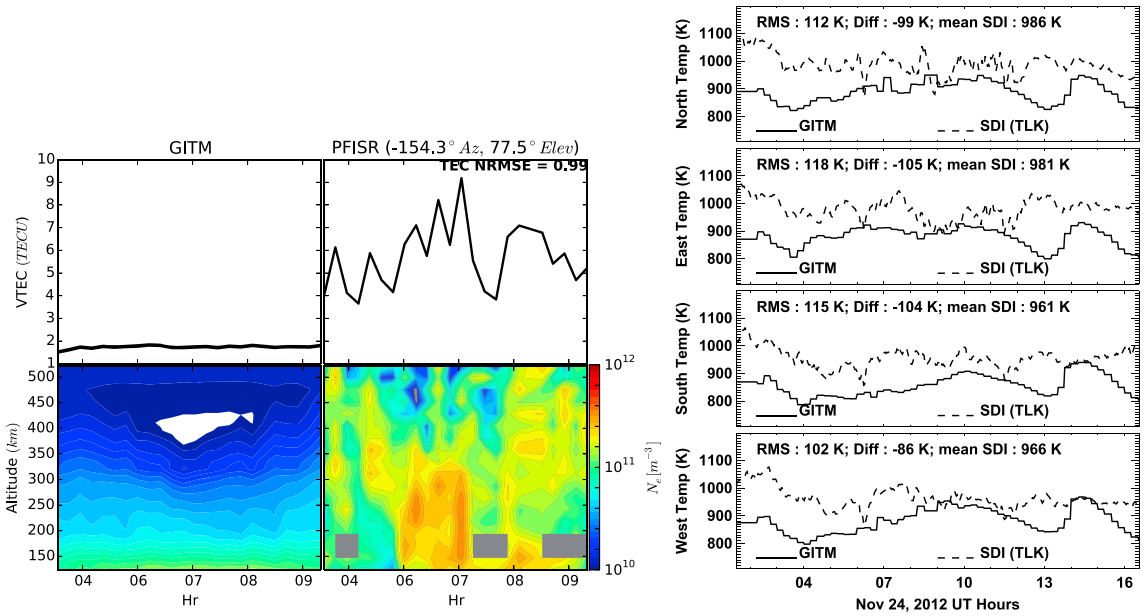

Figure 14. Similar to Figure 6 but for the SdOp run.

east-west errors, suggesting that GITM is better at modeling meridional flows than zonal flows, but this is not necessarily true in all cases. The range of RMS errors found in Table 1 (maximum value-minimum value) in the north-south winds is only 81.8 m/s, where the range in the east-west winds is 115.9 m/s, despite the fact that the maximum and minimum speeds of the wind in both directions are similar. Likewise, the range of the absolute difference errors found in Table 1 is 132.4 m/s in the meridional direction when considering cases where GITM both underestimated and overestimated the SDI winds (for example, the minimum difference value is negative but maximum difference value is positive), and a range of 202.1 m/s in the zonal direction (again, considering both negative and positive values). With such a large spread of RMSE and differences between the north-south and east-west directions, it is clear that the east-west flows are more strongly affected by the changing high-latitude ionospheric drivers than are north-south winds. Again, this is because the drivers considered throughout this study more readily affect the zonal flow patterns of neutrals.

The WN and WOs runs were the closest at reproducing the winds observed by the SDIs throughout the entire night for the zonal neutral winds. In general, each run that used OVATION-SME aurora was better at reproducing the zonal neutral winds at 14:00 UT when there was present, but less intense, auroral precipitation compared to 06:30 UT when the simulations showed strong precipitation. In addition, these runs were able to replicate the slight reversal of westward to eastward and back to westward flows between 60° and 70° near 14:00 UT better than runs that used OVATION Prime aurora.

The baseline run was the most accurate in modeling the meridional neutral winds when compared to SDI instruments, as this run replicated the strong dependence of north-south neutral flow on thermal gradients at every time throughout the night. When GITM correctly modeled the directionality of the meridional neutrals in the other simulations, the flows often aligned with the pressure gradient and ion drag forces and the resulting GITM flows were too fast. This suggests either the ion drag force within the model itself was too large or the model lacked a counteracting force such as viscosity that may act to negate the combined forces. Although it is difficult to discern the reason for this error with the analysis presented here, more detailed studies of this behavior can be performed at a later time.

As opposed to the north-south winds at 06:30 UT, the meridional winds at 14:00 UT were similar between multiple runs due to the lessened auroral activity at this time. Most of the runs showed substantial poleward flows near dawn and dusk and equatorward flows on the nightside, consistent with neutral winds driven by temperature differences between the day and nightside of the planet. In considering both zonal and meridional flows, the simulations were more accurate near 14:00 UT compared to 06:30 UT. The runs

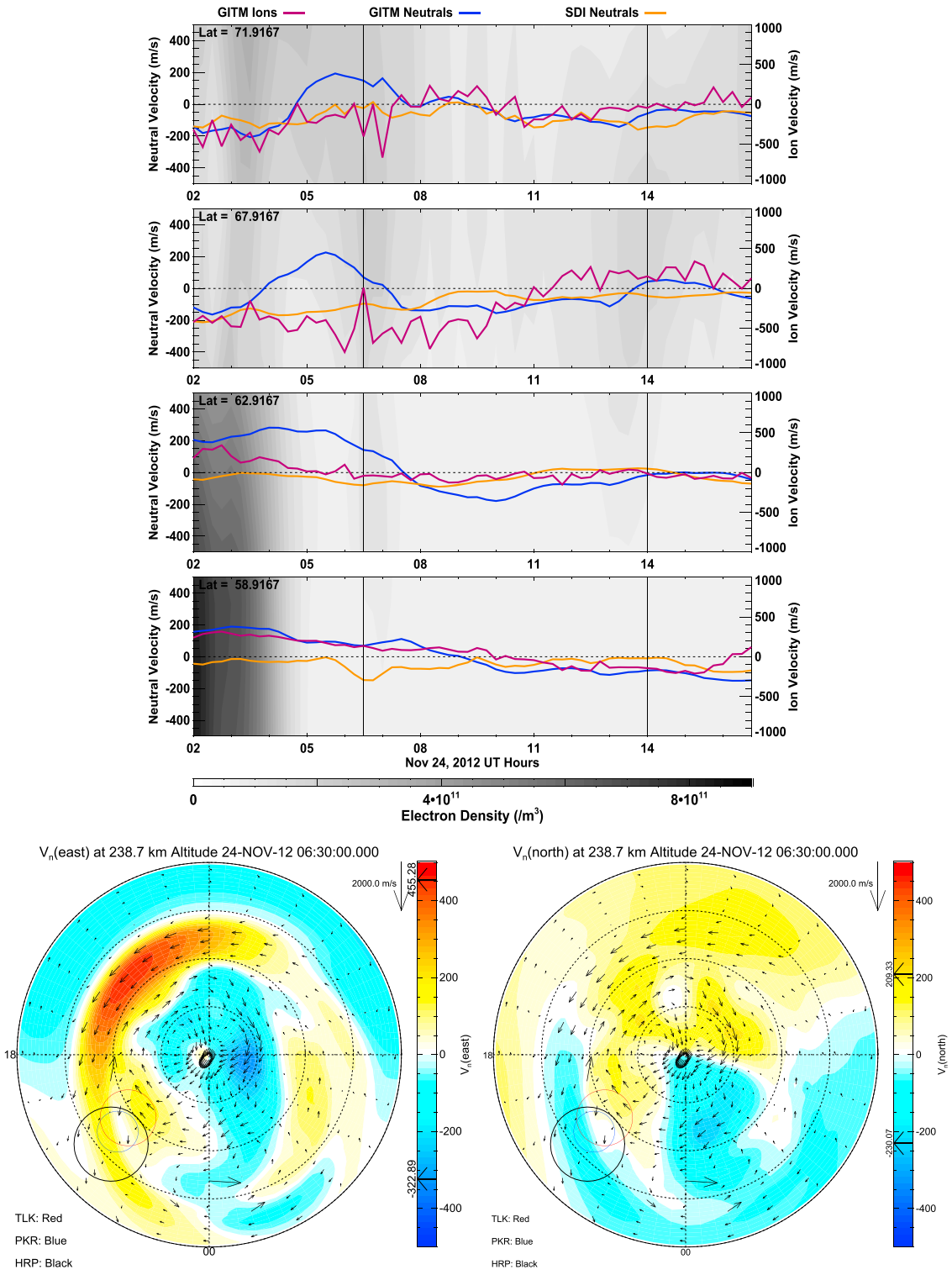

Figure 15. (top and bottom left) Zonal and (bottom right) meridional neutral and ion flow patterns as in Figures 4 and 5 but for the SdOsD run.

demonstrated a strong dependence of the east-west neutral wind behavior on auroral precipitation, although the effect of increased precipitation appeared to have more of an effect on the winds in the premidnight region given that most models were more accurate with Alaska in the postmidnight region near 14:00 UT as opposed to when Alaska was in the premidnight region around 06:30 UT.

In modeling the electron density, runs that used OVATION Prime were not able to replicate the changes in electron density throughout the night that were observed by PFISR for this event. This may be because this particular substorm was not well captured by the IMF conditions that drove the models. The NOAA and OVATION-SME models were able to better capture the large-scale dynamics and apparent spatial characteristics observed during this event. However, to further validate the ability of each auroral model during various ionospheric conditions, future studies might make use of all-sky cameras or special sensor ultraviolet spectrographic imagers to better map spatial and temporal characteristic energies and fluxes of the aurora.

5. Conclusion

This study has presented the results from multiple simulations of a substorm event on 24 November 2012 using the Global Ionosphere-Thermosphere Model. These results included neutral wind velocities located throughout the high-latitude region (focusing mainly above the three Scanning Doppler Interferometers in Alaska), electron densities, and atmospheric temperatures. By changing which high-latitude drivers were used in GITM, each of the parameters listed above was affected and was drastically different from one another. In comparing multiple runs with disparate high-latitude ionospheric drivers, this study has found that the intensified ion-neutral coupling that occurs during times of increased electron density in the ionosphere causes an increase in neutral wind velocities in the zonal direction. In addition, the ability of GITM to replicate the neutral winds over three locations in Alaska is better for times with modest electron precipitation. However, with electron densities that are too high, the neutral wind velocity became too strong and GITM overestimated the magnitude of the observed neutral winds. These findings suggest the following:

1. The electric potential pattern significantly affects the behavior of the high-latitude neutral wind pattern as is evidenced by the differences in the neutral flows when using either statistical (Weimer) or measured (SuperDARN) potential patterns. The differences in neutral wind velocities arising from only changing the type of potential pattern used to drive the model can be larger than 100 m/s in certain high-latitude regions.
2. The auroral precipitation pattern plays a strong role in determining the dynamics of the ion and neutral flows in the high-latitude region. Because the ion and neutral momentum and energy coupling in the high-latitude region are dependent on the electron density, the model must be able to correctly produce the amount of electron density in the system. Incorrect amounts of precipitation lead to inaccurate representations of the neutral flow structure as evidenced multiple times throughout the study.
3. If the ionospheric dynamo is to be used as a boundary condition to the electric potential solver in the model, the latitude of the dynamo boundary must be correctly chosen in order to accurately simulate the ion and neutral flows. A boundary that is too high can cause too much leaking of the electric potential to midlatitudes which affects the neutral wind patterns, but a boundary that is too low may disturb dynamics at lower latitudes.
4. The thermospheric temperature is extremely dependent on both the potential and auroral drivers, with stronger auroral models tending to cause larger temperatures.
5. Because the response of the ionosphere can be considerably different between multiple events, it is difficult to definitively state that a single combination of high-latitude drivers is the most preferable in all instances. For example, although the model run with the Weimer potential and NOAA precipitation patterns was one of the most accurate compared to SDI data in the zonal neutral winds for this event, it was one of the worst in replicating the meridional neutral winds. Similarly, the run with Weimer potential and OVATION-SME auroral precipitation patterns poorly modeled the zonal neutral winds throughout the entirety of the event, but the thermospheric temperature response during the event was very close to the observed thermospheric temperature.

Despite these findings, because accurate and comprehensive descriptions of the high-latitude drivers used in global models are rare, it is difficult to reliably and consistently simulate the thermospheric and ionospheric dynamics that occur at high latitudes. In addition, this lack of observational data makes the validation of neutral wind behavior output by model simulations extremely difficult, especially at specific altitudes or geographic locations. Even with the limited data that can be used to validate the model, the following is clear: without accurate parametrization and specification of ionospheric drivers used in global models, neutral wind model results ranging from mildly inaccurate to unacceptably incorrect will ensue. Therefore, in modeling high-latitude thermospheric winds, a rigorous and comprehensive set of auroral and electric potential drivers must be used to obtain accurate neutral wind flow patterns.

Acknowledgments
This research was funded by NSF grants ATM1138938 and ATM1242787, and NASA grant NNX14AE04G. The interplanetary magnetic field and solar wind data were downloaded from the NASA Coordinated Data Analysis Web site. The hemispheric power was provided by the NOAA Space Weather Prediction Center, and the Auroral Electrojet data were provided by the World Data Center at Kyoto University. All simulation results are available upon request through the Virtual Model Repository at the University of Michigan.

Alan Rodger thanks the reviewers for their assistance in evaluating this paper.

References

Anderson, C., M. Conde, and M. McHarg (2012), Neutral thermospheric dynamics observed with two scanning doppler imagers: 1. Monostatic and bistatic winds, *J. Geophys. Res.*, *117*, A03304, doi:10.1029/2011JA017041.

Aruliah, A. L., D. Rees, and T. J. Fuller-Rowell (1991), The combined effect of solar and geomagnetic activity on high latitude thermospheric neutral winds. Part I. Observations, *J. Atmos. Terr. Phys.*, *53*, 467–483.

Bilitza, D. (2001), International Reference Ionosphere 2000, *Radio Sci.*, *36*, 261.

Chamberlin, P. C., T. N. Woods, and F. G. Eparvier (2007), Flare irradiance spectral model (fism): Daily component algorithms and results, *Space Weather*, *5*, S07005, doi:10.1029/2007SW000316.

Conde, M., and R. Smith (1995), Mapping thermospheric winds in the auroral zone, *Geophys. Res. Lett.*, *22*(22), 3019–3022.

Conde, M., and R. W. Smith (1997), Phase compensation of a separation scanned, all-sky imaging Fabry Perot spectrometer for auroral studies, *Appl. Opt.*, *36*, 5441–5450, doi:10.1364/AO.36.005441.

Conde, M., and R. Smith (1998), Spatial structure in the thermospheric horizontal wind above Poker Flat, Alaska, during solar minimum, *J. Geophys. Res.*, *103*(A5), 9449–9471.

Deng, Y., and A. Ridley (2006), Dependence of neutral winds on convection E-field, solar EUV, and auroral particle precipitation at high latitudes, *J. Geophys. Res.*, *111*, A09306, doi:10.1029/2005JA011368.

Deng, Y., and A. Ridley (2007), Possible reasons for underestimating joule heating in global models: E-field variability, spatial resolution and vertical velocity, *J. Geophys. Res.*, *112*, A09308, doi:10.1029/2006JA012006.

Dickinson, R., E. Ridley, and R. Roble (1984), Thermospheric general circulation with coupled dynamics and composition, *J. Atmos. Sci.*, *41*, 205–219.

Drob, D. P., et al. (2008), An empirical model of the Earth's horizontal wind fields: HWM07, *J. Geophys. Res.*, *113*, A12304, doi:10.1029/2008JA013668.

Emmert, J. T., M. L. Faivre, G. Hernandez, M. J. Jarvis, J. W. Meriwether, R. J. Niciejewski, D. P. Sipler, and C. A. Tepley (2006a), Climatologies of nighttime upper thermospheric winds measured by ground-based Fabry-Perot interferometers during geomagnetically quiet conditions: 1. Local time, latitudinal, seasonal, and solar cycle dependence, *J. Geophys. Res.*, *111*, A12302, doi:10.1029/2006JA011948.

Emmert, J. T., G. Hernandez, M. J. Jarvis, R. J. Niciejewski, D. P. Sipler, and S. Vennerstrom (2006b), Climatologies of nighttime upper thermospheric winds measured by ground-based Fabry-Perot interferometers during geomagnetically quiet conditions: 2. High-latitude circulation and interplanetary magnetic field dependence, *J. Geophys. Res.*, *111*, A12303, doi:10.1029/2006JA011949.

Foster, J., J.-P. St.-Maurice, and V. Abreu (1983), Joule heating at high latitudes, *J. Geophys. Res.*, *88*, 4885–4897.

Fuller-Rowell, T., and D. Rees (1980), A three-dimensional time-dependent global model of the thermosphere, *J. Atmos. Sci.*, *37*, 2545–2567.

Fuller-Rowell, T. J., and D. Evans (1987), Height-integrated Pedersen and Hall conductivity patterns inferred from the TIROS-NOAA satellite data, *J. Geophys. Res.*, *92*, 7606–7618.

Greenwald, R., et al. (1995), Darn/Superdarn: A global view of the dynamics of high-latitude convection, *Space Sci. Rev.*, *71*, 761–796, doi:10.1007/BF00751350.

Hagan, M., J. Forbes, and F. Vial (1995), On modeling migrating solar tides, *Geophys. Res. Lett.*, *22*(8), 893–896.

Hedin, A. (1987), MSIS-86 thermospheric model, *J. Geophys. Res.*, *92*, 4649–4662.

Hedin, A. (1991), Extension of the MSIS thermosphere model into the middle and lower atmosphere, *J. Geophys. Res.*, *96*, 1159–1172.

Hedin, A. (1992), Horizontal wind model (HWM) (1990), *Planet. Space Sci.*, *40*, 556–557.

Hedin, A., N. Spencer, and T. Killeen (1988), Empirical global model of upper thermosphere winds based on atmosphere and dynamics explorer satellite data, *J. Geophys. Res.*, *93*, 9959–9978.

Hedin, A., et al. (1996), Empirical wind model for the upper, middle and lower atmosphere, *J. Atmos. Terr. Phys.*, *58*, 1421–1447.

Hedin, A. E. (1983), A revised thermospheric model based on mass spectometer and incoherent scatter data: MSIS-83, *J. Geophys. Res.*, *88*, 10,170–10,188.

Heppner, J., and M. Miller (1982), Thermospheric winds at high latitudes from chemical release observations, *J. Geophys. Res.*, *87*, 1633–164.

Killeen, T., R. Roble, and N. Spencer (1987), A computer model of global thermospheric winds and temperatures, *Adv. Space Res.*, *7*(10), 207–215.

Killeen, T. L., and R. G. Roble (1984), An analysis of the high-latitude thermospheric wind pattern calculated by a thermospheric general circulation model: 1. Momentum forcing, *J. Geophys. Res.*, *89*, 7509–7522.

Killeen, T. L., and R. G. Roble (1986), An analysis of the high-latitude thermospheric wind pattern calculated by a thermospheric general circulation model: 2. Neutral parcel transport, *J. Geophys. Res.*, *91*, 11,291–11,307.

Killeen, T. L., Y.-I. Won, R. J. Niciejewski, and A. G. Burns (1995), Upper thermosphere winds and temperatures in the geomagnetic polar cap: Solar cycle, geomagnetic activity, and interplanetary magnetic field dependencies, *J. Geophys. Res.*, *100*, 21,327–21,342.

Lathuillère, C., J. Lilensten, W. Gault, and G. Thuillier (1997), Meridional wind in the auroral thermosphere: Results from EISCAT and WINDII-O(^1D) coordinated measurements, *J. Geophys. Res.*, *102*, 4487–449.

McCormac, F., T. Killeen, J. Thayer, G. Hernandez, C. Tschan, J.-J. Ponthieu, and N. Spencer (1987), Circulation of the polar thermosphere during geomagnetically quiet and active times as observed by Dynamics Explorer 2, *J. Geophys. Res.*, *92*, 10,133–10,139.

Meriwether, J. W., J. P. Heppner, J. D. Stolarik, and E. M. Wescott (1973), Neutral winds above 200 km at high latitudes, *J. Geophys. Res.*, *78*, 6643–6661, doi:10.1029/JA078i028p06643.

Mikkelsen, I., T. Jørgensen, M. Kelley, M. Larsen, E. Pereira, and J. Vickery (1981), Neutral winds and electric fields in the dusk auroral oval 1. Measurements, *J. Geophys. Res.*, *86*, 1513–1524.

Millward, G., I. Müller-Wodard, A. Aylward, T. Fuller-Rowell, A. Richmond, and R. Moffett (2001), An investigation into the influence of tidal forcing on F region equatorial vertical ion drift using a global ionosphere-thermosphere model with coupled electrodynamics, *J. Geophys. Res.*, *106*(24), 24,733–24,744.

Mitchell, E., P. Newell, J. Gjerloev, and K. Liou (2013), OVATION-SM: A model of auroral precipitation based on SuperMAG generalized auroral electrojet and substorm onset times, *J. Geophys. Res. Space Physics*, *118*, 3747–3759, doi:10.1002/jgra.50343.

Newell, P., and J. Gjerloev (2011), Evaluation of SuperMAG auroral electrojet indices as indicators of substorms and auroral power, *J. Geophys. Res.*, *116*, A12211, doi:10.1029/2011JA016779.

Newell, P., T. Sotirelis, and S. Wing (2010), Seasonal variations in diffuse, monoenergetic, and broadband aurora, *J. Geophys. Res.*, *115*, A03216, doi:10.1029/2009JA014805.

Niciejewski, R., T. Killeen, and Y. Won (1994), Observations of neutral winds in the polar cap during northward IMF, *J. Atmos. Terr. Phys.*, *56*, 285–295.

Niciejewski, R., T. Killeen, and S. Solomon (1996), Observations of thermospheric horizontal neutral winds at Watson Lake, Yukon Territory (λ = 65°n), *J. Geophys. Res.*, *101*, 241–260.
Rawer, K., D. Bilitza, and S. Ramakrishnan (1978), Goals and status of the International Reference Ionosphere, *Rev. Geophys.*, *16*, 177–181.
Richards, P. G., J. A. Fennelly, and D. G. Torr (1994), EUVAC: A solar EUV flux model for aeronomic calculations, *J. Geophys. Res.*, *99*, 8981–8992.
Richmond, A., E. Ridley, and R. Roble (1992), A thermosphere/ionosphere general circulation model with coupled electrodynamics, *Geophys. Res. Lett.*, *19*, 601–604.
Richmond, A., C. Lathuillère, and S. Vennerstroem (2003), Winds in the high-latitude lower thermosphere: Dependence on the interplanetary magnetic field, *J. Geophys. Res.*, *108*(A2), 1066, doi:10.1029/2002JA009493.
Ridley, A. J., Y. Deng, and G. Tòth (2006), The global ionosphere-thermosphere model, *J. Atmos. Sol. Terr. Phys.*, *68*, 839–864.
Roble, R., and E. Ridley (1994), A thermosphere-ionosphere-mesosphere-electrodynamics general circulation model (time-GCM): Equinox solar cycle minimum simulations (300–500km), *Geophys. Res., Lett.*, *21*, 417–420.
Roble, R., E. Ridley, A. Richmond, and R. Dickinson (1988), A coupled thermosphere/ionosphere general circulation model, *Geophys. Res. Lett.*, *15*, 1325–1328.
Rothwell, P., R. Mountford, and G. Martelli (1974), Neutral wind modifications above 150 km altitude associated with the polar substorm, *J. Atmos. Terr. Phys.*, *36*, 1915–1926.
Schunk, R. W., et al. (2004), Global Assimilation of Ionospheric Measurements (GAIM), *Radio Sci.*, *39*, RS1S02, doi:10.1029/2002RS002794.
Solomon, S., and L. Qian (2005), Solar extreme-ultraviolet irradiance for general circulation models, *J. Geophys. Res.*, *110*, A10306, doi:10.1029/2005JA011160.
Vichare, G., A. Ridley, and E. Yiğit (2012), Quiet-time low latitude ionospheric electrodynamics in the non-hydrostatic global ionosphere-thermosphere model, *J. Atmos. Sol. Terr. Phys.*, *80*, 161–172.
Weimer, D. R. (2005), Improved ionospheric electrodynamic models and application to calculating joule heating rates, *J. Geophys. Res.*, *110*, A05306, doi:10.1029/2004JA010884.
Zhang, S., and G. Shepherd (2000), Neutral winds in the lower thermosphere observed by WINDII during the April 4–5th, 1993 storm, *Geophys. Res. Lett.*, *27*, 1855–1858.